Chapter 2

Fundamentals of transitionally-operating airfoils

The purpose of this chapter is to provide the basic notions required for understanding the different approaches comprising the research. Complying with the schema in Figure 1.1, the narrative is structured following a bottom-up description of realistic approaches. Section 2.1 presents the simplest aerodynamic description, namely the potential flow theory. Section 2.2 adds the effect of viscosity to the previous approach, and constitutes the minimal framework within which transitional structures can be described. Section 2.3 includes the essential concepts for understanding the techniques by which turbulent effects are reproduced experimentally, thus accounting for real freestream conditions, and Section 2.4 does the same with surface-roughness effects. Lastly, Section 2.5 provides the core notions for grasping the numerical approaches undertook herein.

2.1 Potential flow theory as a first description

As mentioned in Chapter 1, the present work focuses on airfoil analysis. Airfoils are specifically shaped bodies that produce a net lift force when immersed in a flow. It is the purpose of aerodynamics to link those three variables together, i.e. to predict how forces are produced as an interrelation between flows and body shapes.

As such, the simplest conception of aerodynamics should only consider two input parameters: one that characterizes the incoming flow, and another that determines the geometry of the airfoil. Figure 2.1a shows this simplified version: the incoming flow is assumed to be two-dimensional, uniform and inviscid, mainly characterised by its velocity far upstream the airfoil (U_∞). The airfoil is considered homogeneous in its spanwise dimension, so that its aerodynamic behaviour can be analysed by studying a two-dimensional cross-section. For the sake of simplicity, the profile is assumed symmetric, with the airfoil's semi-thickness equation being expressed as $y_p(x)$, with x being the streamwise variable. In addition to the profile equation, there are two other parameters that determine the geometry of the configuration: the first is the chordwise dimension (c), which is the length that covers the distance between the leading- and trailing-edges of the airfoil. The second corresponds to the angle-of-attack (α), or the angle between the chord and the incoming flow's direction.

These four parameters, namely $(c, y_p, \alpha, U_\infty)$, constitute a minimal set of variables that is necessary for developing an inviscid aerodynamic approach. The so-called two-dimensional potential theory is the name given to such an approach, and corresponds to the simplest way of undertaking an airfoil analysis [2.1, ch. 4]. This theory allows performing certain calculations and deriving some preliminary conclusions about the general aerodynamic behaviour of airfoils. In particular, it shows that the net lift force experienced by the airfoil, namely l, is a consequence of the different pressure distributions developed along its upper and lower surfaces. Figure 2.1c shows a schematic of such distributions, which are represented by the arrows perpendicular to the surface at each point. The lower surface of the airfoil, i.e. the one that stands below the chord line, is named the pressure-side of the airfoil, as the flow causes a pressure that pushes it upwards.

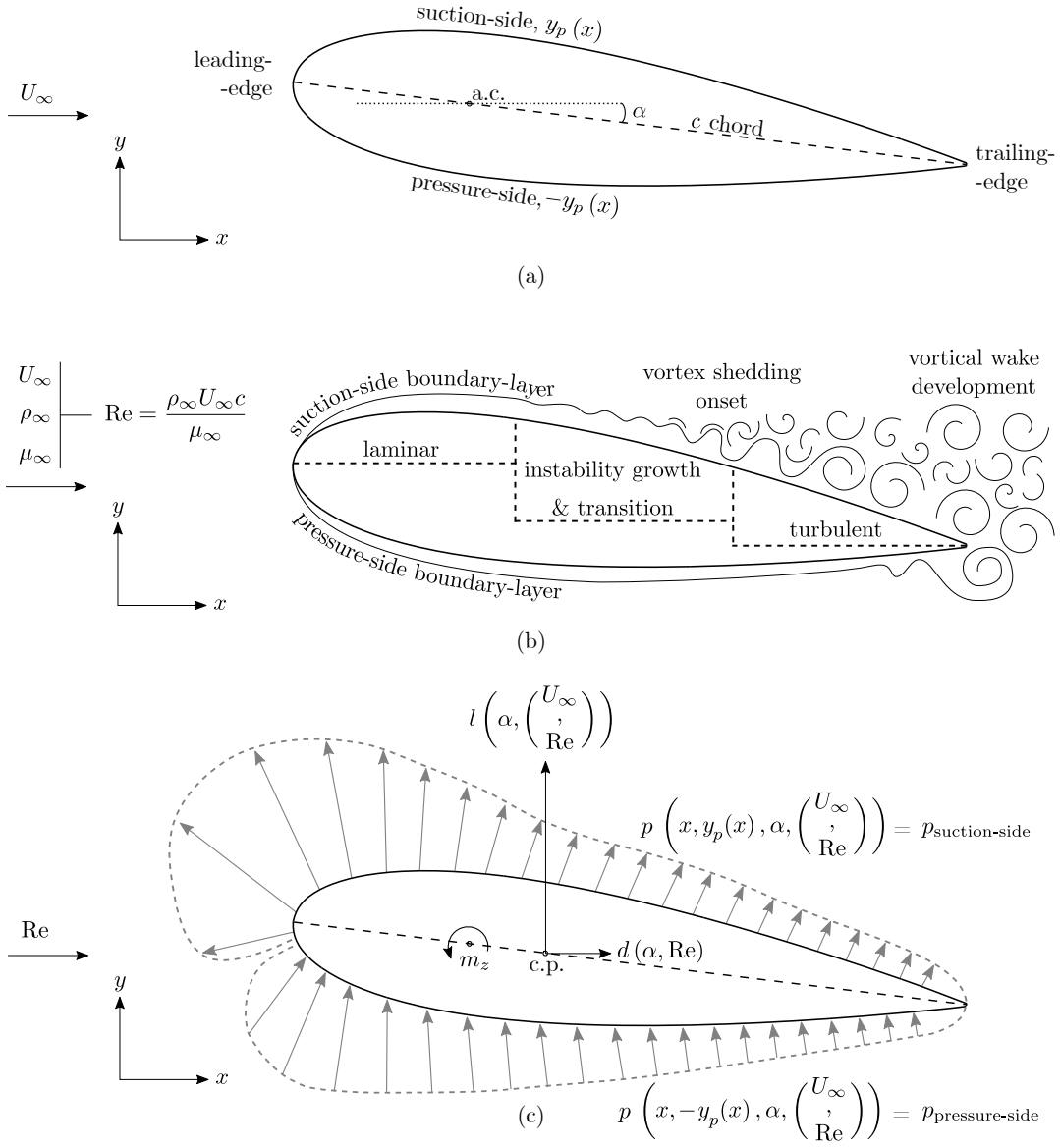

Figure 2.1: set of parameters and notions for describing: (a) the potential paradigm; (b) the clean-flow paradigm; (c) the loads, momenta and distributions entering both the potential and the clean-flow descriptions.

The upper surface is named the suction-side of the airfoil, as the upwards push is coming from a pressure distribution that induces a suction at the surface. In potential flow theory, these pressure values depend on the geometry of the configuration and the velocity of the flow, which is why the generic equation of the distributions is $p = (x, y_p(x), \alpha, U_\infty)$. The lift force results from integrating the difference of the suction- and pressure-side distributions along the chordwise dimension:

$$l(\alpha, U_\infty) = \int_c (p_{\text{pressure-side}} - p_{\text{suction-side}})\, \mathrm{d}x \ , \tag{2.1}$$

and it is a magnitude that depends on the angle-of-attack and the velocity of the flow. Besides, the convention in aerodynamics is to employ dimensionless variables and, instead of pressure distributions and lift forces, it is more usual to use their respective coefficients. The pressure coefficient is the ratio of the pressure value and the dynamic pressure upstream ($q_\infty = \rho_\infty U_\infty^2/2$) or, equivalently:

$$p = q_\infty \cdot c_p \ . \tag{2.2}$$

The lift force is related to its coefficient in an analogouos way:

$$l = q_\infty \cdot c \cdot c_l \ , \tag{2.3}$$

and, hence, Equation (2.1) can be written thusly:

$$c_l = \int_c \left(c_{p_{\text{pressure-side}}} - c_{p_{\text{suction-side}}}\right) \mathrm{d}x' \ , \tag{2.4}$$

where $x' = x/c$ is the dimensionless chordwise parameter.
Insofar the lift magnitude addresses a resultant force, it is applied at a given point of the airfoil. Such a point is the center of pressure (c.p.), and is where the force-vector is located in Figure 2.1c. Due to the lift force, the airfoil experiences a pitching moment along the $z-$axis, namely m_z, which is depicted at a $c/4$ distance from the leading-edge in Figures 2.1a and 2.1c. This other point is known as the aerodynamic center (a.c.)[(1)], and its feature is that the pitching moment is independent from the angle-of-attack when referred to it.

2.2 Clean-flow paradigm

The achievements of potential flow theory, taking into account that it is the simplest conceivable approach in aerodynamics, are not few: it predicts the pressure distributions and the lift force, as well as defining the center of pressure and the aerodynamic center. However, the simplifying assumptions that the theory presumes have their drawbacks. In particular, the approach does not provide a correct description of the drag force. What's more, the theory predicts that such a force, which results from projecting the pressure distributions in the stremwise direction, is null for uniform and steady flow conditions (D'Alembert's paradox), precisely the ones given above. This conclusion contradicts empirical observations, and it shows the necessity of modifying the theory for deriving a better aerodynamic description.
The step forward comes from including the viscous forces, thus dropping the inviscid flow consideration. Air, as any other fluid, has a property known as viscosity (μ_∞, far upstream) that shows its resistance against shearing forces. The larger the viscosity, the higher the force required for shearing a fluid, and the more it behaves as a solid-like body.
Viscous effects introduce two main features into the aerodynamic description of the flow. First, they resolve D'Alembert's paradox due to two contributions: one of them is the viscous drag, or the drag that the airfoil experiences due to the shearing effect of viscosity. The other is the pressure drag, resulting from a modified distribution of pressures which results in a separation of the flow towards the trailing-edge of the airfoil,

(1) this only applies in subsonic flows; supersonic ones have their a.c. at the midchord.

causing a pressure jump between the leeward and rearward of it. These two contributions amount to a net drag force (d) that opposes the direction of the flow, whose expression is analogous to the lift force:

$$d = q_\infty \cdot c \cdot c_d \ , \tag{2.5}$$

with c_d being the drag coefficient.
The second feature that viscous effects introduce has to do with the modification of the momentum equation [2.1]. In potential flow theory, such an equation expresses the balance between two terms: the convective forces, which are the ones that a fluid has due to its velocity, and the pressure forces. When including viscosity, an extra term is added to the equation. As the governing mechanism of aerodynamics is the convective force, the relevance of the viscous term is made apparent by estimating its value and comparing it to the convective one. This ratio between convective and viscous forces is named the Reynolds number (Re), and is defined as:

$$\mathrm{Re} = \frac{\rho_\infty U_\infty c}{\mu_\infty} \ , \tag{2.6}$$

where ρ_∞ stands for the density of the fluid far upstream. The reference to the chordwise dimension is not casual: it means, first of all, that the characteristic length of the analysis is the chord of the airfoil. Secondly, it is an indirect way of telling that the viscous forces develop along such a chord. The partial success of the potential flow theory comes from the fact that viscosity is negligible throughout the flowfield, except in a region near the surface of the airfoil where its effect is comparable to that of the convective forces. Such a region is known as the boundary-layer.
Insofar the boundary-layer is a viscous phenomenon, it is related to the Reynolds number in two ways. First of all, its relevance is quantified by estimating how far the viscous effects reach, i.e. by comparing the thickness of the boundary-layer (δ) to the chord of the airfoil: the ratio δ/c can be show to be proportional to $\mathrm{Re}^{-1/2}$. The larger the Reynolds number, the thinner the boundary-layer as a consequence of a lesser relevance of the viscous term. Secondly, it was already shown by Osborne Reynolds himself that the Reynolds number allows classifying the fluid motions into three different flow regimes: laminar, turbulent and transitional [2.2]. The laminar regime corresponds to relatively small Reynolds numbers, which means that the viscous effects are significant and, due to their dissipative nature, they damp possible perturbations occurring within the flow. This results in an ordered motion of the fluid, with the streamlines being configured in a set of staggered layers. On the contrary, large Reynolds numbers imply that the particles own higher kinetic energies, and the dissipative effect of viscosity becomes unable to sustain the energised perturbations. As a consequence, a chaotic motion of the particles ensues, and the resultant state is turbulent. Intermediate Reynolds numbers result in a configuration where the flow transitions from the laminar state to the turbulent one, and is named the transitional regime accordingly.
Despite such a classification, there is no such thing as a universal correlation between Reynolds number intervals and flow regimes. For internal flows such as pipe streams, Reynolds established that the flow becomes fully turbulent for $\mathrm{Re} \approx 10^3$ [2.2]. In external flows, such as those developed around airfoils, it is common to assume that the regime is laminar for $\mathrm{Re} < 10^4$, becoming entirely turbulent at $\mathrm{Re} = 10^6 - 10^7$; the interval $10^4 < \mathrm{Re} < 10^6$ may be considered as the one where transitional effects prevail [2.3, 2.4]. Airfoil configurations subjected to $\mathrm{Re} < 5{\cdot}10^5$ are said to operate in low-Reynolds numbers [2.4].
Additionally, the statement that an airfoil is operating in a particular flow regime is to be understood properly. Figure 2.1b shows that boundary-layers develop along both the suction- and pressure-sides of the airfoil, and they do so differently. The chord-based Reynolds number is a surrogate for the overall behaviour of the airfoil, but does not take into account factors such as the pressure gradient to which the flow is subjected. At the suction-side, such a gradient is positive or adverse, with the boundary-layer facing a larger pressure resistance while travelling downstream. The opposite is true at the pressure-side, where the boundary-layer finds a favourable pressure gradient and is not as perturbed as in the suction-side. As each boundary-layer faces different conditions, it is dubious to state that they share the same flow regime. Furthermore, the boundary-layer originates at the leading-edge of the airfoil, and proceeds downstream convected by the freestream flow. At each chordwise stage, the local Reynolds number

is $\mathrm{Re}_x = \rho_\infty \cdot U_\infty \cdot x/\mu_\infty$, with x being the distance travelled from the leading-edge. As Re_x increases proportionately to x, the boundary-layer may undergo regime changes, beginning in a laminar state and ending in a turbulent one.
Such is the configuration shown in the suction-side boundary-layer of Figure 2.1b. On this respect, stating that an airfoil operates in a transitional regime when the chord-based Reynolds number is between $10^4 < \mathrm{Re} < 10^6$ has a specific interpretation: it means that the transitional region covers a significant chordwise extent. In applications such as aircrafts flying at high subsonic speeds, for which $\mathrm{Re} = 10^6 - 10^7$, the kinetic energy of the particles is so large, and the boundary-layer so thin, that it undergoes a rapid transition from laminar to turbulent. Such a transition occurs in a short chordwise extent near the leading-edge, and the overall suction-side of the airfoil may be assumed to face turbulent conditions. However, MAVs or mid-scale wind turbines operate at $10^4 < \mathrm{Re} < 10^6$. At those Reynolds numbers, the extents of the different flow regions along the suction-side match the ones pictured in Figure 2.1b. A transitionally-operating airfoil discernibly develops such three regions along its suction-side.
Thus, shifting from potential theory to viscous flow has the following implications: it allows including the drag force in the aerodynamic description, and defines the Reynolds number as a combined flow- and geometry-related parameter that substitutes the U_∞ variable present in the simpler approach. This description, in which airfoil load- and presure-coefficients are analysed under viscous, uniform, steady and two-dimensional conditions, will be called the clean-flow paradigm hereon, and the flows reproduced under such a paradigm, clean configurations.
In addition to those parameters, it is usual to define the aerodynamic efficiency, or simply efficiency (E), as the ratio between the lift and the drag of an airfoil:

$$E = \frac{l}{d} = \frac{c_l}{c_d} \ . \tag{2.7}$$

The efficiency may be interpreted as a parameter that measures the output/input ratio of an aerodynamic system. The lift force is responsible for sustaining an aircraft in the air or getting a power output from a wind turbine. Instead, the drag force must be balanced by the engines' thrust of the aircraft, or acts by decelerating the rotary motion of the wind turbine. In both cases, the efficiency parameter is an indicator that shows how well the system behaves from the standpoint of an output/input ratio of energies. In the former case, a higher efficiency means that a lower fuel consumption is required for undertaking a flight. In the second one, large E values stand for higher power production rates. As such, the efficiency stands as a synthetic parameter of the loads that is well-suited for complementing a proper aerodynamic analysis. As sketched in Figure 2.1c, the purpose of the clean-flow paradigm is to determine the evolution of the four aerodynamic outcomes with the two input parameters, namely $(c_l, c_d, E, c_p\,(x, y_p)) = f\,(\alpha, \mathrm{Re})$.

2.2.1 Transitional flows and laminar separation bubbles

The purpose of analysing transitionally-operating airfoils has a well-founded rationale behind. Laminar and turbulent regimes are well understood from the standpoints of basic and applied research paradigms, but this is not so for the transition process [2.5]. Studies are still undertaken upon such simplified geometries as flat plates, with the aim of elucidating what are the basic mechanisms that govern the laminar-to-turbulent passage [2.6, 2.7]. This does not mean that applied works do not exist. Indeed, studies about the transitional characterization of airfoils have been carried out at the experimental level [2.8–2.10], the numerical one [2.11, 2.12], or even following the combined experimental-numerical approach [2.13, 2.14]. Furthermore, some of the studies, besides characterising the aerodynamic behaviour, aim at acting upon the airfoil by means of passive [2.15–2.17] or active control techniques [2.18–2.20]. The proliferation of such studies highlights two key points: the first is the already mentioned separation between basic- and applied-research approaches. Despite the incomplete understanding of the physical processes, characterization efforts persevere based on an accepted view of the basic aerodynamic structures comprising transition. The second point is that the interest on applied research about transition indicates a lack of complete understanding, even on the characterization stage, which justifies undertaking further studies on this particular topic.

As mentioned, there is an accepted view about the phenomenology of transitional flows. Such a view considers that the laminar-to-turbulent process combines phenomena of those two regimes in a particular way. Either upon flat plates or along curved surfaces such as airfoils, the characteristic feature of transitional flows is the development of an aerodynamic structure termed laminar separation bubble (LSB hereon).
Figure 2.2 shows an LSB formed upon a generic surface. The flow, coming from left to right, travels laminarly near the leftmost region of the surface, as represented by the set of staggered streamlines. Factors such as the curvature of the surface or the adverse pressure gradient make the boundary-layer encounter an ever-growing resistance to flowing. Eventually, the velocity profile becomes unstable and the flow separates from the surface. This occurs at the $s - s''$ stage, which is named the separation line. Beyond such a line, the flow evolves in the form of a separated shear-layer, and undergoes transition some distance downstream. For the sake of clarity, the line $t - t''$ represents a simplistic view in which transition occurs at a fixed stage, although, actually, it spans across a finite chordwise extent. After becoming turbulent, the particles of the shear-layer are re-energised, beginning to overcome the viscous forces and producing turbulent eddies within the flow. The shear-layer, if it's lying sufficiently close to the surface, can reattach to it at the $r - r''$ line. Unlike the separation line, the reattachment one is known to be highly unstable and dependent on the freestream conditions [2.21]. The turbulent boundary-layer resulting from the reattachment phenomenon evolves downstream in a spreading manner, with the flow streamlines diverging noticeably when compared to their laminar counterparts and the turbulent eddies becoming larger as they travel along the surface.

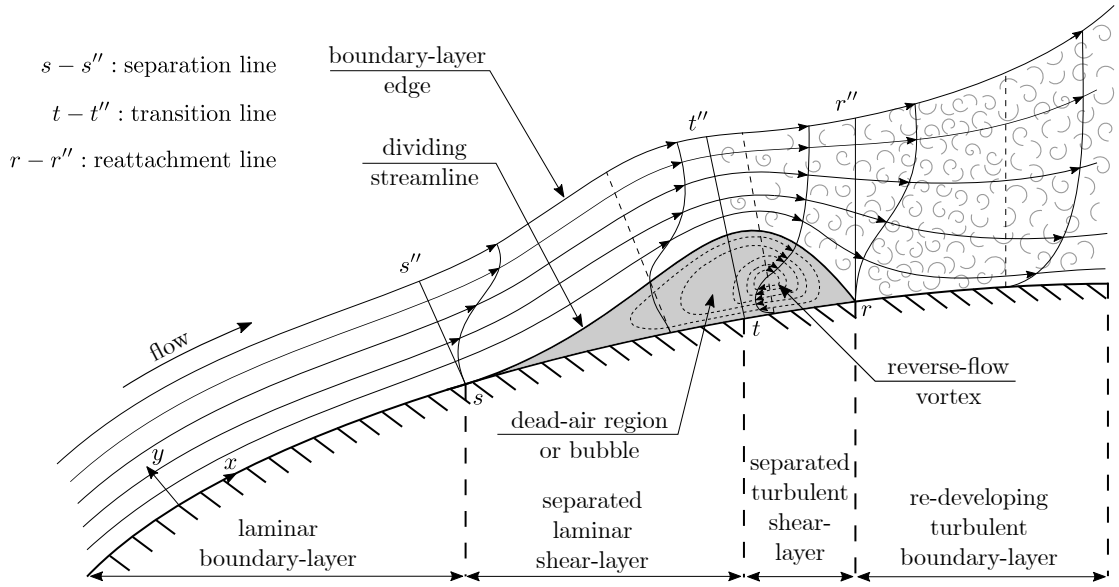

Figure 2.2: schematic of an LSB formed along a generic surface. Adapted from [2.22].

The described phases that the boundary- and shear-layers undergo are delimited by the dashed vertical lines, which split the surface into the laminar, transitional and turbulent regions. The shear-layer that undergoes transition between the separation and reattachment lines develops a region of dead air beneath it. Such air moves in a relatively slower, recirculating motion that is swept by the freestream flow at its upper boundary and travels in the opposite direction near the surface. It is this pocket of recirculating air, which is governed by a reverse-flow vortex located within, what is known as an LSB.
The LSB induces several changes on the aerodynamic behaviour. Originately, the term was employed for giving a possible explanation of the strange behaviour that certain airfoils show at stalling [2.23]. Stalling

is a phenomenon that occurs at moderately high angles-of-attack, when the steep geometrical gradient imposed by the leading-edge of the airfoil makes the air unable to surround it following its contour. As a result, the flow detaches from the surface a short distance downstream the edge. The airfoil loses its ability to generate a pressure difference between its suction- and pressure-sides, and adopts a bluff-body-like behaviour, producing a reduced lift and an increased drag. The LSB is said to cause a particular type of stalling, that in which the change of behaviour occurs in a sudden way, showing an abrupt loss of lift and growth in drag. Other stalling mechanisms may also occur, and the main parameter determining the type of stalling is known to be the relative thickness of the airfoil (t/c, with t being the maximum thickness) [2.24]. This leads to the classification of stalling types shown in Figure 2.3.

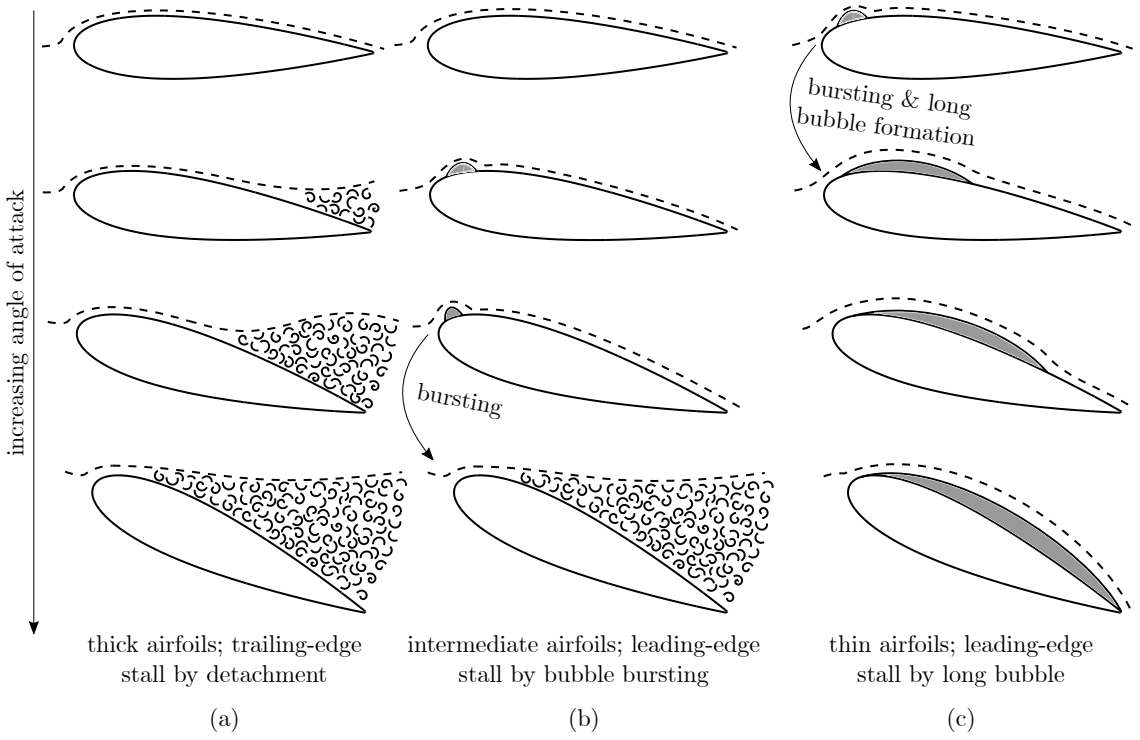

Figure 2.3: stalling mechanisms depending on the relative thickness of the airfoils, attending to the classification given by McCullough & Gault [2.24]. Adapted from [2.1, ch.8−pp.234-238].

From left to right, the depicted airfoils follow a decreasing trend of relative thicknesses. Figure 2.3a corresponds to a thick airfoil case ($t/c \gtrsim 20\%$), which shows a trailing-edge-type stalling. The way in which such a stalling occurs is shown when looking at the pictures of the column in a top-down manner, as they represent an increasing trend on the angles-of-attack. As observed, the flow begins to detach from the rear-side of the airfoil, and such a detached region covers a progressively larger portion of the chord as α increases. In contrast, airfoils with intermediate thickness values (Figure 2.3b, $10\% \lesssim t/c \lesssim 20\%$) develop a leading-edge LSB at low angles-of-attack. Such a bubble shrinks and moves upstream with increasing α values. Beyond a certain angular configuration, the bubble bursts and produces an abrupt stalling. This causes sudden variations in the aerodynamic loads, which may result in a loss of control of the overall system. The fomer case, instead, shows a much milder variation on the lift and drag evolutions, as the stalled region progresses slowly with the angle-of-attack. That's why, preferably, the second stalling type

is to be avoided. The third type corresponds to thin airfoils (Figure 2.3c, $t/c \lesssim 10\%$), which produce an LSB structure at low angles that enlarge and turn into a long bubble at higher α values. Eventually, the bubble covers the entire suction-side, causing a flatter pressure distribution along it. This diminishes the lift outcome and, as the bubble causes a larger frontal area to be exposed to the freestream flow, it also increases the drag value. Although this stalling mechanism may sound as progressive as the former one, the LSB constitutes an unstable structure that is liable to undergo a bursting process at any time, which may lead to load-jumps similar to those experienced by intermediate-thickness airfoils [2.25, 2.26]. Anyhow, neither the relative thickness values nor the stalling mechanisms are as fixed as described above. It is more usual to have combinations of such mechanisms depending on the specific airfoil geometry and the particular set of freestream conditions [2.24].
Besides stalling, transitionally-operating airfoils are known to show the phenomenon of aerodynamic hysteresis. Indeed, hysteresis and stalling are closely related phenomena. As described, stalling occurs at moderately high angles-of-attack. For a given airfoil subjected to a clean configuration, let α_{stall} be the angle at which it stalls. The angles standing beyond α_{stall} constitute the so-called post-stall region, where the c_l behaviour is not as predictable as for pre-stall conditions, whereas the c_d shows a monotonously increasing trend in agreement with the bluff-body condition of the airfoil. The hysteresis phenomenon manifests when attempting to recover pre-stall conditions by decreasing the angle-of-attack. Experimental observations show that such conditions are not regained by resetting the α_{stall} configuration. It turns necessary to lower the angle-of-attack further, until reaching a value $\alpha_{\text{recov.}} < \alpha_{\text{stall}}$ that causes the recovery. When it occurs, the airfoil regains its streamlined-body condition, and both c_l and c_d return to their pre-stall values. The different behaviours of the aerodynamic coefficients between $\alpha_{\text{recov.}}$ and α_{stall}, depending on the sign of the airfoil's angular variations, are what constitute the hysteresis cycle. This cycle is mostly noticeable when the stalling mechanism is governed by an LSB structure, as occurs with intermediate-thickness airfoils. Indeed, the abrupt coefficient jumps that correspond to both stalling and recovery are ascribed to an unstable behaviour of the bubble and its bursting process [2.27], with the hysteresis phenomenon not ensuing in thicker airfoils subjected to a trailing-edge-type stalling.
Lastly, low$-\alpha$ configurations are known to be affected by the LSB structure as well. The slow, recirculating flow within the bubble produces a flatter pressure distribution on that region, in contrast to the inviscid situation in which the abscence of an LSB leads to a monotonous pressure recovery along the suction-side of the airfoil. As both the length and the chordwise position of the bubble vary noticeably with the angle-of-attack, the potential and viscous pressure distributions differ. The potential theory predicts a linear relationship between c_l and α at low angular configurations, namely $c_l(\alpha) = 2\pi\alpha$ [2.1, ch.4$-$pp.107-111]. The bubble breaks such a relation, mainly because of the different pressure distributions causing severe c_l deviations from the linear trend [2.10].
The LSB-related effects described above, those that alter the linear trend at the low$-\alpha$ region and modify the stalling and hysteresis behaviours at moderately higher angles-of-attack, have been exposed in an exclusively geometry-dependent manner. Insofar the bubble is a transitional structure, its development is largely affected by the freestream conditions. Indeed, the characteristic feature of the transitional regime is that the aerodynamic coefficients are highly sensitive to the Reynolds number [2.3]. Such a sensitivity does not mean that the bubbles are inherently unstable. At a fixed pair of (α, Re) values, the LSB formed upon an airfoil is a stable structure. But slight variations in either of the parameters causes a radical reconfiguration of the aerodynamic coefficients, affecting the overall behaviour severely. That's why it turns necessary to analyze the airfoils in terms of both the angular configurations and the Reynolds numbers. As expressed before, characterising the behaviour of transitionally-operating airfoils subjected to the clean-flow paradigm means specifying the functional relations $(c_l, c_d, E, c_p(x, y_p)) = f(\alpha, \text{Re})$.

2.2.2 Characteristic curves

The characteristic curves refer to the plots that are used as the baseline of the analysis, i.e. as the conventional way of representing the functional relations described above. The clean-flow paradigm includes two input parameters, namely the pair (α, Re). From those, it is standard practice to choose the angular variable

for constructing the curves. The evolutions of the lift, drag and efficiency parameters are represented as $c_l\,(\mathrm{Re}) - \alpha$, $c_d\,(\mathrm{Re}) - \alpha$ and $E\,(\mathrm{Re}) - \alpha$ curves, respectively. The pressure distributions, additionally, depend on the dimensionless chordwise position x'. This requires the construction of two additional datasets, i.e. $c_p\,(\alpha) - x'$ and $c_p\,(\mathrm{Re}) - x'$, in order to cover the parametrical space altogether.
The distinction made above between the representation modes of the c_l, c_d and E variables, on the one hand, and the c_p distributions, on the other hand, highlights the different nature of each set of parameters. The former constitute global variables, in the sense that they address an outcome of the airfoil as a whole; that's why they do not depend on the chordwise position. The pressure distributions own a more local nature and, as such, they may provide insights on the specific mechanisms governing the behaviour of LSBs. The link between the local and global approaches is given by Equation (2.4): the lift coefficient is obtained by integrating the suction- and pressure-side c_p difference along the chord. Anyhow, this distinction between global and local variables is relevant insofar it allows splitting the analysis into a mainly behavioural (global variables) and a preeminently phenomenological (local variables) aspects.

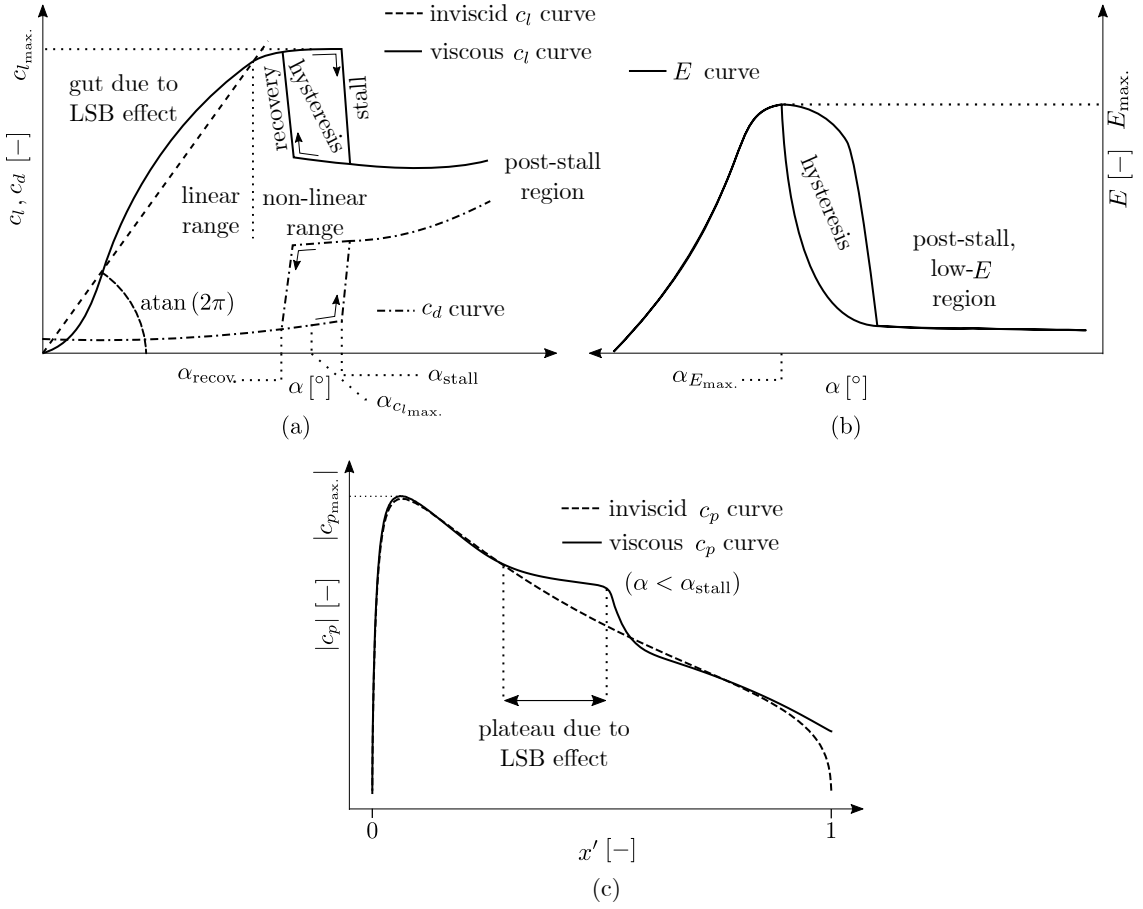

Figure 2.4: characteristic curves of a generic, transitionally-operating airfoil at a specific, pre-stall angle-of-attack; (a) $c_l - \alpha$ (both for potential and clean-flow paradigms) and $c_d - \alpha$ curves; (b) $E - \alpha$ curve; (c) suction-side $c_p - x'$ distributions for potential and clean-flow paradigms.

The shapes adopted by the characteristic curves of a generic, transitionally-operating airfoil are shown in Figure 2.4. For illustrative purposes and without loss of generality, the curves of the global variables are plotted for an unspecified, fixed Reynolds number. Likewise, the $c_p - x'$ plots merely show the suction-side distribution (that in which the LSB structure is formed) for an unstalled angle-of-attack and the same unspecified Reynolds number for which the global curves are obtained. Figures 2.4a and 2.4b illustrate the evolutions of global variables. The angular range of these plots covers the pre- and post-stall regions, so that both the low$-\alpha$ phenomenology and the stalling and hysteresis mechanisms are captured. Figure 2.4a shows the $c_l - \alpha$ and the $c_d - \alpha$ curves. The $c_l - \alpha$ ones are plotted for both the potential and clean-flow approaches. The potential approach merely reproduces the linear $c_l - \alpha$ relationship at low angles-of-attack, with the slope of the line matching the 2π factor as predicted by the theory. The clean-flow paradigm is shown to diverge noticeably from such a trend, with the LSB effect causing either lower-than-potential c_l values at the lowest angular configurations, or higher ones at larger angles. In any case, such deviations are merely illustrative, and the precise deviations are to be determined by the characterization process. At larger angles the curve begins to saturate, with c_l not increasing as rapidly with α as in the initial zone. This marks the beginning of the non-linear range and, thus, the end of applicability of the potential theory. In parallel, the c_d curve undergoes a monotonous increase along this angular range, although its evolution is much milder than the $c_l - \alpha$ one, mainly because of the streamlined nature of the airfoil that reduces the c_d value to the small contribution of the viscous drag. Eventually, the airfoil reaches its maximum lift point ($c_{l_{\text{max.}}}$) and, further beyond, stalling occurs. The stalling angle may coincide with the maximum lift angle, i.e. $\alpha_{\text{stall}} = \alpha_{c_{l_{\text{max.}}}}$, but this need not always be the case. When stalling, both c_l and c_d undergo sudden jumps, according to the described mechanism based on bubble bursting. The post-stall region is characterised by a monotonous c_d increase, as a larger frontal area is exposed to the flow and the airfoil behaves like a bluff body, with the pressure drag contribution being the dominant one. For decreasing angles-of-attack, pre-stall conditions are regained at $\alpha_{\text{recov.}} < \alpha_{\text{stall}}$, and the loopholes that show up between those two angles reflect the hysteretic behaviour of the airfoil.
Figure 2.4b shows that the behaviour of the efficiency parameter follows closely the $c_l - \alpha$ evolution, especially at low angular configurations. This is because the drag values evolve mildly within the pre-stall region, which turns the shape of the c_l curve into the main qualitative aspect driving the efficiency evolution. In contrast, saturation and stalling may be strongly modulated by the drag evolution, mainly due to its sharper increase within the non-linear region. In fact, the angle at which the maximum efficiency is obtained may not coincide with the maximum lift angle, i.e. $\alpha_{E_{\text{max.}}} \neq \alpha_{c_{l_{\text{max.}}}}$, as the smooth lift variations during saturation contrast with the steeper drag gradients therein. Anyhow, the hysteresis cycle gets equally reflected on the $E - \alpha$ curves, and the usual post-stall region shows a nearly-constant, low-valued efficiency evolution.
Figure 2.4c represents suction-side pressure distributions for a given Reynolds number and a pre-stall angle-of-attack, obtained according to both the potential theory and the clean-flow paradigm. The $y-$axis scaling shows absolute values, as the suction-side coefficients are negative when measured by differential pressure probes referenced to upstream flow conditions. Whereas the neighbourhoods of the suction peak, represented by the maximum c_p value, are predicted equally by both approaches, the clean-flow paradigm develops a plateau-like region at the midchord that does not agree with the monotonous trend of the potential theory. That's the effect of the dead-air region within the bubble, which produces a nearly-constant region of pressure recovery. The extent and location of this plateau are expected to change appreciably when varying the flow configuration, being responsible for the observed deviations of the c_l value from the predictions of the potential theory. However, the suction-side distribution is to be complemented with its pressure-side counterpart for obtaining the whole picture of the $c_p - x'$ evolution.

2.3 Turbulent-flow paradigm

The conditions under which LSBs have been said to develop in Section 2.2.1 represent artificial flow configurations. Such flows may be achieved in carefully designed wind tunnels aimed at reproducing steady

and uniform air currents. However, these clean configurations do not show the complexity of genuine flows encountered in real conditions. If an airfoil is designed by following the guidelines derived from a characterization performed under the clean-flow paradigm, its behaviour may vary substantially from the expected one when it is placed in its operation site. A thorough characterization should look for reproducing the real conditions that the airfoil is presumed to face. A first step towards obtaining such conditions is to consider that the flow is not as steady and uniform as in clean configurations. Indeed, transitionally-operating devices such as MAV wings, turbomachinery vanes or portions of mid- and large-scale wind turbine blades are known to meet turbulent flow conditions [2.28–2.31].
Stating that the incoming flow is turbulent has implications that are to be understood properly. First of all, freestream turbulence is not to be considered as a synonym for turbulent flow regime. Despite the turbulent character of the flow, the boundary-layer of the airfoil may adopt the aspect shown in Figure 2.2, developing both laminar and transitional regions before turning turbulent itself. The LSB may persist as a characteristic flow structure even when turbulence is included, and its effects on the evolution of the bubble are to be studied accordingly.
Second of all, the inherently chaotic nature of turbulent flows is assumed to be characterizable. Such flows are conceived as being formed by a continuous stream of eddies. An eddy is a whirling structure of a given size that rotates with a specific velocity, very much like the spirally-shaped arrangements shown within the turbulent boundary-layer portion in Figure 2.2. Linking the size and rotation of the eddies to measurable turbulent properties should be the task of a theory required as a baseline for performing the characterization of the flowfield, previous to the characterization of the airfoil itself.
Providing the core concepts of such a theory is the first aim of this section. A simple technique for the experimental reproduction of theory-compliant turbulent flows is presented in parallel. Ultimately, the purpose is to modify the functional relations $(c_l, c_d, E, c_p\,(x, y_p)) = f\,(\alpha, \mathrm{Re})$ so that the right hand-sides of the equations include a relevant turbulent parameter.

2.3.1 HIT and grid-generated turbulence

Turbulent motion stems from an excess of kinetic energy of the particles, which makes them overcome the dissipative action of viscosity. As a result, the particles mingle with each other in a chaotic way, and the ordered streamlines observed in a laminar motion turn into eddy-like structures. Nevertheless, keeping a flow turbulent requires a continuous influx of energy for maintaining the excess of kinetic energy. Viscous dissipation acts ubiquitously and, in the abscence of an energetic input, it leads to a decaying process by which turbulence is ultimately suppressed.
This process was first described by Kolmogorov and termed "the energy cascade" [2.32]. Such a cascading prescribes a multi-scalar eddy hierarchy that comprises three levels, each of them corresponding to a characteristic length of the eddies and being responsible for a particular energetic mechanism. The largest and smallest scales produce and dissipate the turbulent energy, and are termed ℓ_0 and η, respectively. Within the intermediate scale, known as the intertial range and termed ℓ, the energy gets transferred from larger to smaller scales. According to this scheme, a flow-perturbing agent that injects the required energy induces the largest eddies, which, apart from owning a size ℓ_0, they flow with a characteristic velocity V_{ℓ_0}. Their associated Reynolds number (Re_{ℓ_0}), frequency (f_{ℓ_0}) and energy (ε) are:

$$\mathrm{Re}_{\ell_0} = \frac{V_{\ell_0}\ell_0}{\nu} \gg 1\ ,\ f_{\ell_0} \sim \frac{V_{\ell_0}}{\ell_0}\ ,\ \varepsilon \sim \frac{{V_{\ell_0}}^3}{\ell_0}\ . \tag{2.8}$$

The largeness of the Reynolds number above means that the dissipative action of viscosity is not relevant if compared to the convective term of the eddies. However, viscosity does play a role as an energy-transmitting agent towards ever-decreasing structures. The feature of the intermediate range is that neither an injection nor a dissipation of energy takes place, but merely a transmission. Thus, the Reynolds number remains large when associated to characteristic lengths $\ell < \ell_0$ and velocities V_ℓ, i.e. $\mathrm{Re}_\ell = V_\ell \ell/\nu \gg 1$. For that to

happen, the velocities and frequencies of the intermediate scales must fulfill:

$$\begin{aligned} \frac{{V_\ell}^3}{\ell} \sim \frac{{V_{\ell_0}}^3}{\ell_0} \implies V_\ell \sim V_{\ell_0} \left(\frac{\ell}{\ell_0}\right)^{1/3} \ll V_{\ell_0} \ , \\ f_\ell \sim \frac{V_\ell}{\ell} \sim \frac{V_{\ell_0}}{\ell_0} \left(\frac{\ell_0}{\ell}\right)^{2/3} \sim f_{\ell_0} \left(\frac{\ell_0}{\ell}\right)^{2/3} \gg f_{\ell_0} \ . \end{aligned} \tag{2.9}$$

Hence, large and slow-rotating eddies are stretched into smaller and faster-whirling ones until the so-called Kolmogorov scale (η) is reached. The feature of such a scale is that the viscous effects become as relevant as the convective ones, i.e. $\mathrm{Re}_\eta \sim 1$, and the turbulent kinetic energy gets finally dissipated.
The above description shows that the only requirement for producing a turbulent flowfield is to own an energy-injecting device. On experimental grounds and, more precisely, in wind tunnel facilities, it is a common practice to employ grids for such a purpose, producing what is known as grid-generated turbulence [2.33]. In grid-generated turbulence, the incoming flow undergoes a sudden shear when passing through a perpendicularly-oriented grid. Such a shear injects the energy required for developing a turbulent flowfield downstream. The abscence of any other source of energy within the tunnel makes turbulence decay progressively due to the cascading process. The simplest way for mathematically describing such a decay is to assume that the flow is statistically homogeneous and isotropic. The resultant flow is named homogeneous and isotropic turbulence (HIT) accordingly, and is successfully described by the HIT theory [2.34].

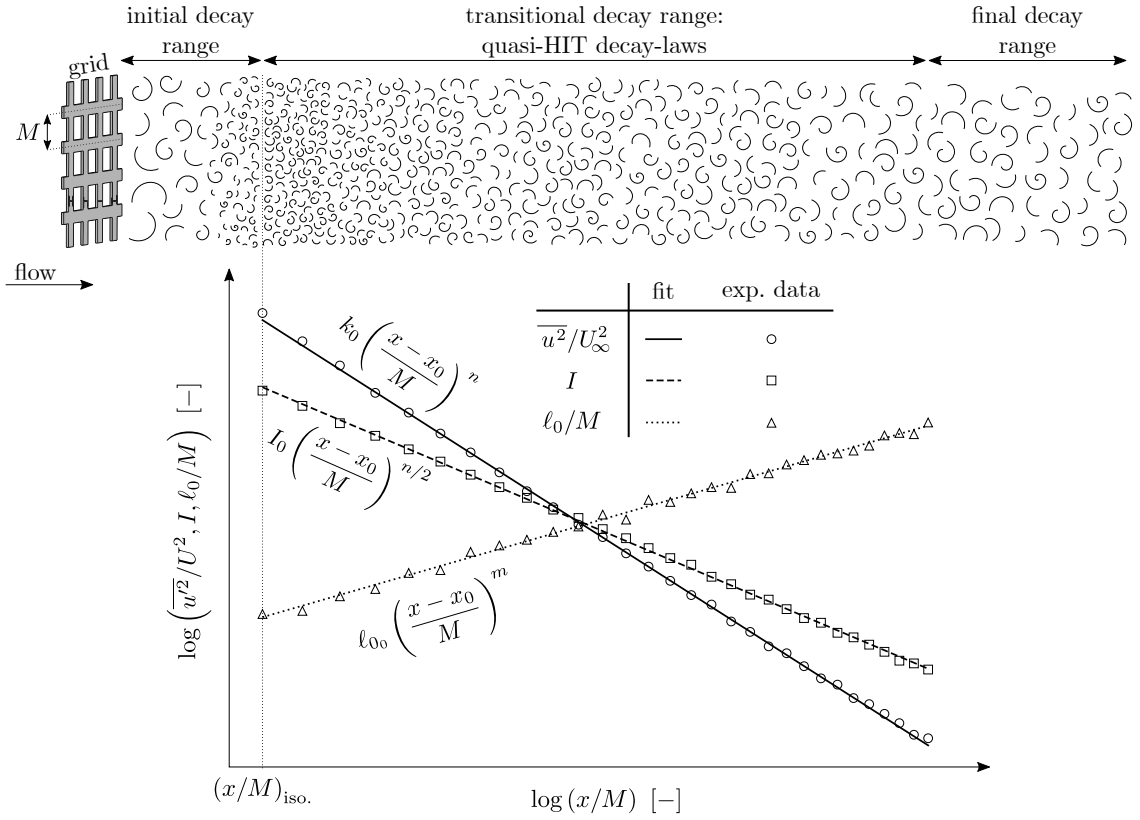

Figure 2.5: streamwise evolutions of the power-law decays of turbulent variables.

The main derivation of the HIT theory is that the turbulent kinetic energy (k) evolves downstream the grid following a power-law decay. Putting the focus on the kinetic energy is essential, as it represents the magnitude by which Kolmogorov describes the cascading process. The definition of k requires considering that, in turbulent flows, it is a common practice to decompose any velocity component of a fluid particle into two main contributions. One of such splittings is the Reynolds decomposition which, in case of the streamwise component (u), reads thusly:

$$U = \overline{U} + u \ , \tag{2.10}$$

where $\overline{U}$ represents a temporally-averaged mean velocity and u stands for the turbulence-induced fluctuating part. Considering that the same expression holds for the spanwise (v) and vertical (w) components, the turbulent kinetic energy adopts the form:

$$k = \frac{\overline{(u)^2} + \overline{(v)^2} + \overline{(w)^2}}{2} \overset{\text{iso.}}{=\!=} \frac{3}{2}\overline{(u)^2} \ , \tag{2.11}$$

where the last equality holds because of the accepted isotropic nature of the flow, which means that, statistically, the velocity fluctuations are identical regardless of the considered direction ($u = v = w$).
The circular-symbol dataset in Figure 2.5 shows the experimentally-measured decay of kinetic energy in a log−log plot. The fit of such a dataset, represented by the solid line, is what HIT theory predicts. The $x-$axis of the plot represents a dimensionless streamwise variable, namely x/M, where M stands for the mesh-parameter that, for a squarely-shaped grid, is the distance between the centerlines of two adjacent rods, as shown in the sketch at the top of the figure. Thus, the evolution of the kinetic energy is plotted against the number of downstream mesh-distances, beginning from a specified stage $(x/M)_{\text{iso.}}$ at which the flow becomes homogeneous and isotropic after an initial region of non-HIT conditions. Donwstream $(x/M)_{\text{iso.}}$, the straight descending line traced by the kinetic energy shows that its evolution follows a power-law decay.
The determination of the kinetic energy decay plays a relevant role on favouring the cascading description of grid-generated turbulence. However, it is not a dimensionless quantity, and flows with different velocities sharing similar turbulent dynamics cannot be discerned properly on the basis of their k values. For that purpose, the turbulent intensity (I) is defined, which reads:

$$I = \frac{\sqrt{\frac{\overline{(u)^2}+\overline{(v)^2}+\overline{(w)^2}}{3}}}{U_\infty} \overset{\text{iso.}}{=\!=} \frac{\sqrt{\overline{(u)^2}}}{U_\infty} \ . \tag{2.12}$$

The intensity parameter has two advantages: first, it is dimensionless, which allows comparing turbulent flows. Second, it has a physical meaning: it is the ratio between turbulent fluctuations and the upstream velocity, thus measuring the strength of the eddies and playing the role of a characterizable parameter. As it is defined, the intensity is proportional to the square-root of the kinetic energy and, consequently, its log−log representation corresponds to a descending straight line with half the slope of the k evolution.
Apart from the strength of the eddies measured by the parameter, it is usual to characterize their integral length-scale which, in an isotropic approach, is no more than ℓ_0. The length of an eddy, from a statistical standpoint, is obtained by computing the autocorrelation function of the velocity fluctuations:

$$\ell_0 = U_\infty \int_0^\infty \frac{\overline{u\,(t)\,u\,(t-T)}}{\overline{u^2}} \mathrm{d}T \ . \tag{2.13}$$

where T represents a time-lag or displacement period. Such a function acquires a unit value for a zero time-lag, i.e. $T = 0$, and decreases monotonously towards 0 for higher lags. An eddy, if understood as an structure that encompasses a set of fluid particles in a coherent manner, will last as long as the autocorrelation function remains positive. On practical grounds, the integral is taken between 0 and a value for which the integrand first becomes negative. The HIT prediction of ℓ_0 is that it evolves towards larger values downstream the grid, as a consequence of the largest eddies tending to match the characteristic length of the system within which they are developing, namely the wind tunnel. When passing through

the grid, the flow is torn down until reaching the characteristic size M and acquiring a high turbulent kinetic energy. Afterwards, two processes take place: first, the cascading process by which the energy of the largest eddies are transferred to smaller ones, leading to the decay of turbulence. Second, the progressive coalescence of the largest eddies that give rise to the increasing ℓ_0 trend. The process represented at the top of the figure corresponds to the growth of the integral length-scale. With all, the power-law decays followed by these three parameters are:

$$k = k_0 \left(\frac{x - x_0}{M}\right)^n, \quad I = I_0 \left(\frac{x - x_0}{M}\right)^{n/2}, \quad \ell_0 = \ell_{0_0} \left(\frac{x - x_0}{M}\right)^m . \tag{2.14}$$

In the expressions above, the exponents n and m, the pre-factors k_0, I_0 and ℓ_{0_0} and the so-called virtual origin x_0 are to be obtained from a turbulence characterization procedure. The exponent n is well-predicted by the HIT theory [2.34, 2.35], and the pre-factors are no more than the values at which the lines cut the ordinate axis. However, the virtual origin is a more elusive concept. The usual interpretation is that it addresses the streamwise location at which fully turbulent conditions ensue [2.36]. Anyhow, it is a parameter that affects the evolution of the decay curves critically, thus requiring a careful calculation [2.36, 2.37]. Lastly, the power-law expressions just hold within the intermediate streamwise region at which HIT conditions are assumed to hold. Neither the initial nor the final decaying intervals comply with such conditions, and delimiting those regions is also a task of the turbulence characterization procedure.

2.3.2 Turbulent conditions in real flows

The benefit of employing HIT as a description of turbulence is that its characterization consists in determining two scalar variables: the intensity and the integral length-scale. The medium in which the majority of transitionally-operating airfoils work, such as MAV wings or wind turbines blades, is the atmosphere. The relations that exist between the turbulent parameters and the operation altitude have been extensively studied, and the accepted correlations are gathered in international standards [2.38, 2.39], as well as depicted on Figure 2.6.

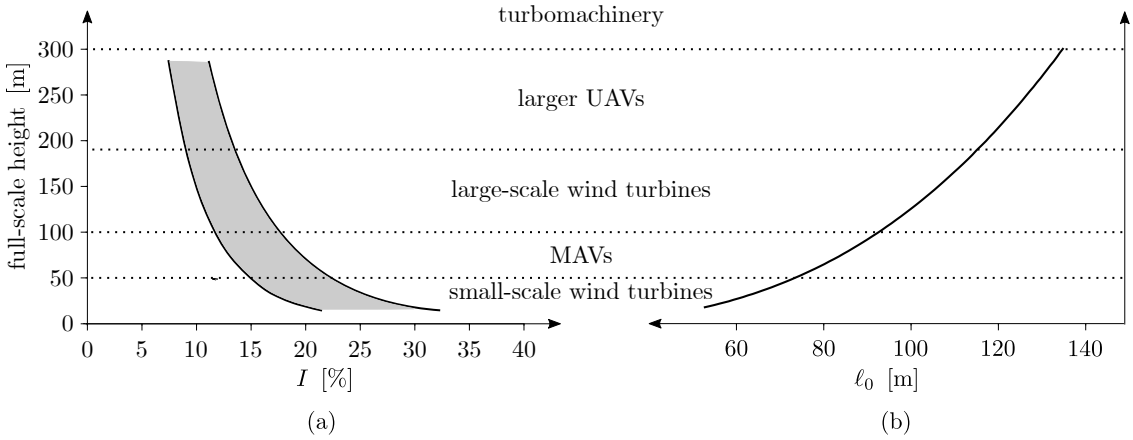

Figure 2.6: evolution of turbulent parameters with atmospheric height; (a) turbulent intensity, I; (b) integral length-scale, ℓ_0; adapted from [2.39].

Figure 2.6a shows a shaded area corresponding to the possible values that the intensity can acquire with increasing heights, represented by the $y-$axis. The general trend, though, is for the intensity to decrease

at higher altitudes. In contrast, Figure 2.6b shows that ℓ_0 increases with height. The dotted horizontal lines delimit regions which, according to bibliography, typical aerodynamic devices operate: small-scale wind turbines [2.40], MAVs [2.30, 2.41], large-scale wind turbines [2.31, 2.42], UAVs [2.29] and, finally, turbomachinery-related applications(2) [2.28, 2.43, 2.44].
Experimentally, it is feasible to obtain intensity values below 15 %, but length-scales as large as 40 m are not reproducible, mainly because, at the very least, the mesh-parameter should have those dimensions. There are two ways for overcoming this limitation: either producing properly-scaled atmospheric-boundary-layers (ABLs), or ignoring the mismatch between the reproduced and genuine length-scales, focusing merely on the intensity parameter. This last approach seems justified according to the recent study of Jafari et al. [2.45], who mention that the characteristic parameter is obtained by comparing ℓ_0 to the chord of the airfoil, i.e. ℓ_0/c. For $\ell_0/c \gg 1$, the airfoil is not affected by the dynamics of the integral eddies, as they are much larger than the airfoil itself. Instead, the relevant scales are the smaller ones for which $\ell/c \approx 1$. This allows dropping the length-scale variable from the analysis, insofar the experimentally reproduced eddies are comparable to the chord of the airfoil. With all, the functional relations that correspond to the turbulent-flow paradigm adopt the form $(c_l, c_d, E, c_p\,(x, y_p)) = f\,(\alpha, \mathrm{Re}, I)$.

2.4 Rough-flow paradigm

Turbulence allows modifying the flow conditions for including real effects. The other aspect of the configuration, namely the geometrical one, requires the consideration of roughness effects for becoming realistic. Airfoils never follow the mathematical curve that defines their surface in an exact manner: first of all, manufacturing defects are unavoidable beyond the precision of the employed machines, which already introduce a certain level of surface-roughness [2.46, 2.47]. Second of all, environmental agents are likely to cause a damage on the airfoil. The presence of these agents, as well as their specific nature, depends on the operation-site of the airfoil. Devices placed in tropical areas are probable to suffer from a larger exposure to insects [2.48, 2.49], as well as facing heavy-rain periods that affect their aerodynamic behaviour [2.50, 2.51]. Those in desertic areas will show dust accumulations and erosion [2.52, 2.53], whereas turbomachinery-related applications are liable to be affected by fuel and oil depositions and thermally-induced corrosion [2.54]. Apart from the presence of environmental agents, the operation period correlates directly with the damage received by the airfoil, with higher surface areas being affected more severely as time goes by [2.52, 2.55].
The type of surface damage described above is termed herein as stochastic roughness. Its treatment is statistical, as it does not represent a purposefully induced roughness, but one that stems from non-deterministic sources. The other type of roughness that airfoils may incorporate is intended to flow-control purposes: it consists of specifically-designed elements that are placed strategically, so that an improvement of the aerodynamic behaviour results. Such a discrete-roughness-based approach is employed as a passive flow-control technique. It constitutes the counterpart of stochastically-induced roughness, both in its deterministic nature (the discrete elements are parametrised by design) and in the effects it induces. As in the previous section, the aim is to show how the functional relations $(c_l, c_d, E, c_p\,(x, y_p)) = f\,(\alpha, \mathrm{Re})$ can incorporate roughness-related parameters on their right-hand sides.

2.4.1 Stochastic roughness

The original studies about the effects of stochastic roughness on fluids were undertook in channeled flows [2.56, 2.57]. Such studies provided a normalised plot for representing the pressure-loss caused by rough walls, which is depicted on Figure 2.7. The plot is a log−log representation, putting the pressure-loss factor (λ) against the Reynolds number. There are two relevant aspects on the plot: first of all, it is divided into three flow regimes, with the flow behaviour being classified as hydrodynamically smooth, transitional or rough. The analogy with the laminar-transitional-turbulent scheme is evident: indeed, both classifications

(2) although these constitute internal flows, and may not be subjected to the conditions predicted by the plots.

are based on the Reynolds number. In case of Figure 2.7, the smooth region corresponds to low Reynolds numbers, and its main feature is that the pressure loss depends exclusively on Re (it is the well-known relation obtained by Moody [2.58]). On the contrary, the rough region is located at high Reynolds numbers, and λ is a function of the roughness parameter (r/k) alone, with r being the radius of the pipe and k an average height of the rough elements; the higher they are (the lower the r/k value), the greater the pressure loss, showing the detrimental effect of roughness. The transitional region stands between them, with the pressure loss depending on both Re and r/k.

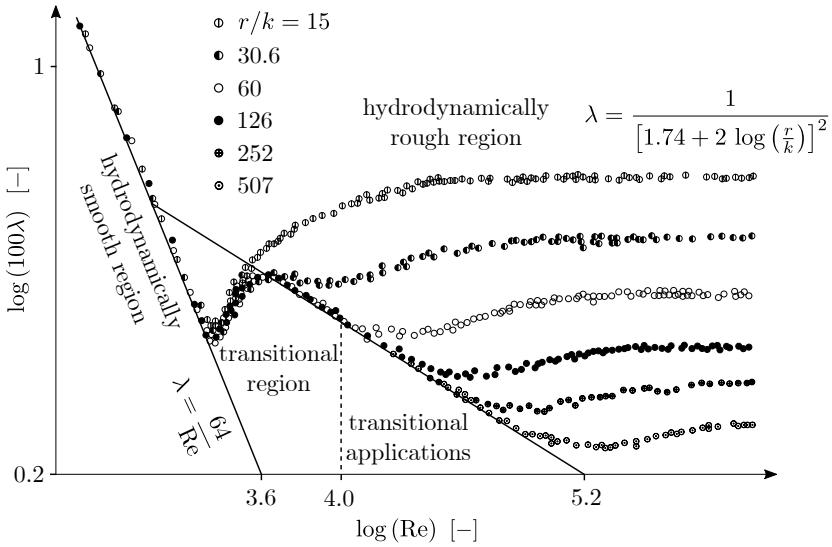

Figure 2.7: roughness-based flow regimes, adapted from [2.56].

The second relevant aspect has to do with the hydrodynamic nature of the plot, as well as with the roughness parameter itself. These two features indicate that the studies were performed under flow conditions that differ substantially from airfoil configurations. Indeed, the analysed flows corresponded to liquid streams in channels, the walls of which were covered with different sandgrain papers for reproducing the roughness effect. Although the description provided in Figure 2.7 remains valid currently, the task of further studies has been to translate it into the aerodynamic realm [2.59–2.61]. Substituting the pipe-radius variable (r) by the airfoil chord has been the first step, leading to the definition of a new parameter termed the equivalent sandgrain roughness, and defined as $k_s = k/c$ [2.61]. However, there is a lack of consensus when it comes to defining a standard procedure for measuring k [2.54]. The variables required for characterising a stochastic roughness distribution are not clear, with studies favouring the usage of conventional roughness parameters such as the average height [2.52, 2.55], and others highlighting the need for considering factors like the density of the distribution or the shape of the elements [2.59, 2.60, 2.62].
Anyhow, the experimental reproduction of rough conditions has not varied since the original studies. It consists on attaching a sandgrain paper to the airfoil, covering the surface portions that are mostly affected by roughness [2.52, 2.54, 2.55]. Instead of sandgrain paper, it is possible to employ analogous materials such as zig-zag bands or patterned motifs [2.63, 2.64]. When adopting this approach, the characterization of k_s is usually reduced to measuring the average height of the elements $(k_s = h/c)$, and the surface extent covered by roughness (d_r/c) accounts for the effect of the operation period, with larger areas being ascribed to longer periods [2.52, 2.65]. The functional relations are expressed as $(c_l, c_d, E, c_p\,(x, y_p)) = f\,(\alpha, \mathrm{Re}, k_s, d_r/c)$.
A schematic view of the factors that constitute the description of stochastic roughness is given in Figure 2.8. The upper part of the figure shows that airfoils of transitionally-operating applications are affected

by both manufacturing- and environmentally-induced roughness effects. Whereas the first are unavoidable, the second depend on the operation site of the devices, and not all of them are reproducible experimentally. Indeed, attaching a sandgrain paper to the airfoil constitutes an addition of material, which corresponds to effects such as insect contamination, dust accumulation or fuel deposition. However, phenomena like spallation, corrosion or dust erosion require eliminating certain material from the surface, which the approach adopted herein does not contemplate. The fact that two distinct processes, namely debris accumulation and material elimination, lead to substantially different aerodynamic consequences has been reported in recent studies [2.66, 2.67]. The lower part of the figure specifies how stochastic roughness is characterised and reproduced experimentally, and the variables considered by the roughness models.

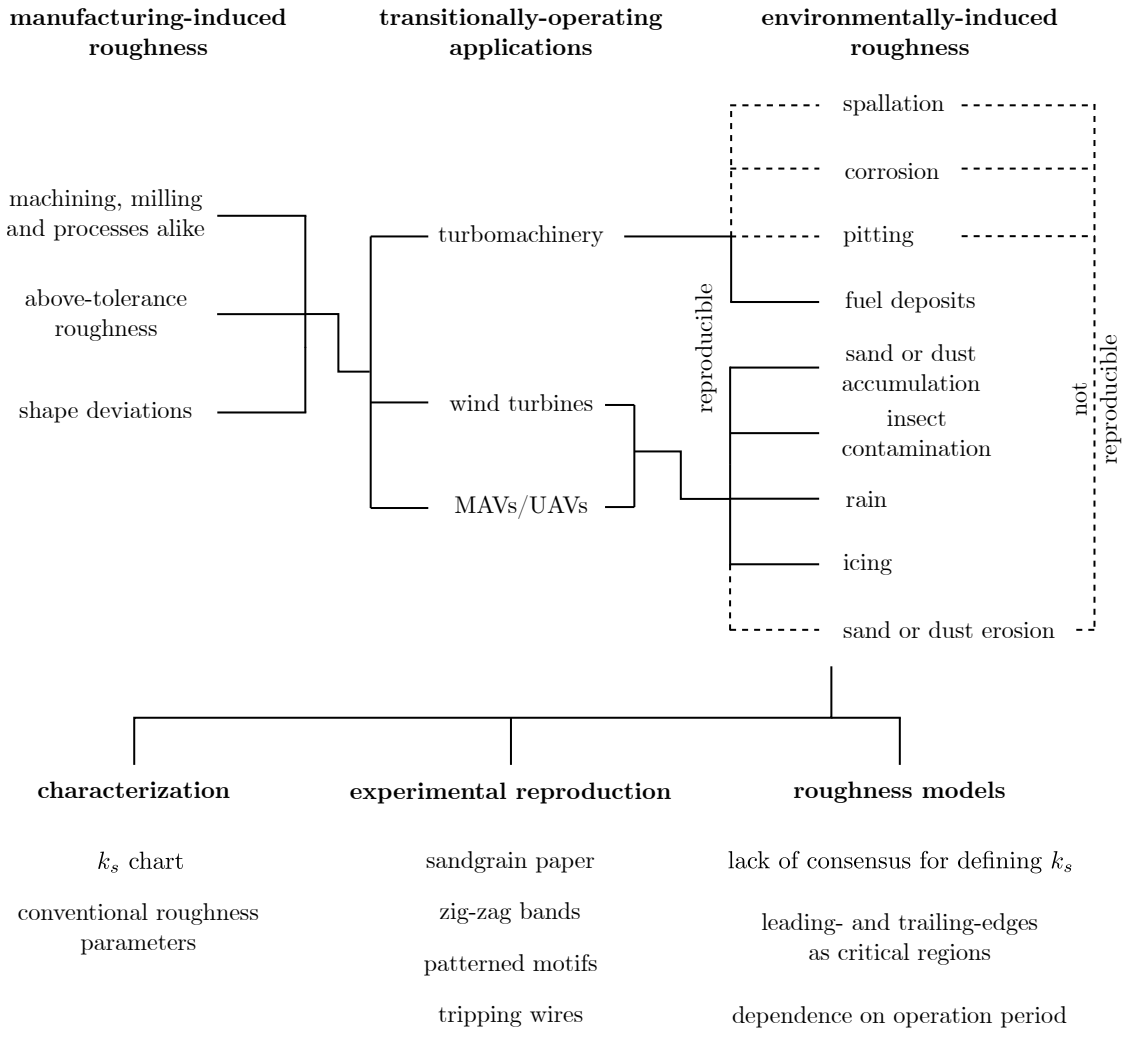

Figure 2.8: overall description of stochastic roughness.

2.4.2 Discrete roughness

The discrete-roughness-based approach constitutes a passive flow-control technique. Vortex generators are probably the paradigm of this technique, aimed at avoiding the separation of the flow and inducing a lift enhancement [2.68]. Other studies have analysed the effectiveness of zig-zag stripes, dimples or wires with the same purpose [2.63, 2.64, 2.69]. However, lift enhancement is not the only benefit that can be obtained from equipping the airfoil with rough surfaces. Drag reduction is also possible, especially the one induced by turbulent effects. Riblets refer to biomimetichally-inspired designs that imitate the dermal properties of animals such as sharks or dolphins [2.70]. Materially, they look like wrinkled or grooved surfaces, and they are usually placed near the trailing-edge of the airfoil, where the boundary-layer has already become turbulent [2.71, 2.72]. The dead-air regions produced on such grooves do not contribute to the drag, which is solely affected by the turbulent flow that travels along the cusps; thus, the amount of wet surface is reduced, and the drag force diminishes accordingly [2.73].

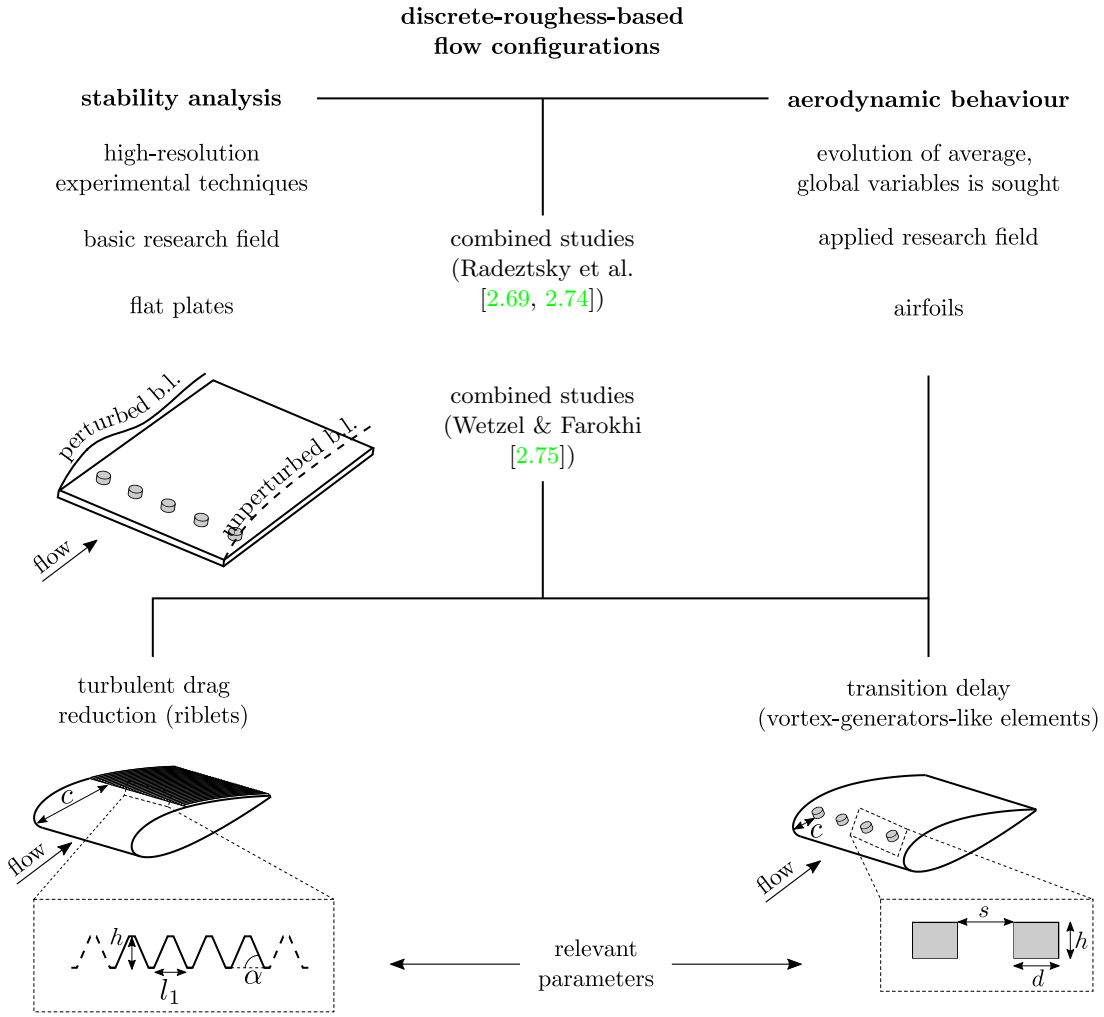

Figure 2.9: overall description of discrete roughness.